Measurement and Characterization of Monodisperse and Bidisperse Dense Granular Flows in a Split-Bottom Cell

Matthew Petersen

Submitted in partial fulfillment of the requirements of the degree of

Bachelor of Science with Honors in Mechanical Engineering

Brown University, School of Engineering

3 May 2017

Prof. David Henann (Advisor) .....

Prof. Christian Franck (Reader) .....

Honors Committee Chair .....

Contents

[1]The work in this appendix was carried out as part of a senior-level engineering design capstone project. This appendix, in report form, was submitted as the deliverable for that capstone requirement.

Abstract

This study aims to establish sound methods for experimental validation of granular flow continuum models. Granular materials are prevalent in industry and nature, and significant inefficiencies are incurred due to the lack of a predictive modeling capability. Robust continuum models for flowing granular materials are currently not available, and reliable experiments are essential to the development and validation of such models. In this work, the split-bottom cell geometry is used to investigate both monodisperse and bidisperse granular systems. Phenomena of interest include shear banding and size segregation. Digital-image-correlation (DIC) methods are used to extract displacement and hence velocity data from video recordings of the flow surface in the monodisperse case. In the bidisperse case, bright region density is used as a proxy measure for large/small grain population ratios.

Acknowledgements

I would like to thank Dr. David Henann, my thesis advisor, for the opportunity to work on this project. I've been involved with this work in some way or another since sophomore year, and Dr. Henann's support, advice, and guidance throughout the process has been invaluable. I would also like to thank Dr. Christian Franck, my reader, who has enabled this thesis and whose research group has been an excellent resource. In particular, I would like to thank Alexander Landauer and Mohak Patel, whose help on matters optical and imaging-related has been essential to the completion of this process. I would also like to offer thanks to all of the members of the Henann Lab, in particular Daren Liu and Michael Jandron, who have let me use their computers to run jobs at odd hours (and sometimes not-so-odd hours) and who have provided me with helpful analytical advice. I would also like to acknowledge and express gratitude to all of the faculty of the School of Engineering who have kept me engaged and inspired throughout my time here. Finally, I would like to thank my family and friends for their support throughout this project.

Chapter 1

Introduction

Granular materials are frequently used in many applications: cereal grains, sands and gravels, and many other bulk products are transported in a granular form. In industry, these materials are the second-most-handled material after water, and have enormous economic importance [1]. Predictive models for granular flow are crucial to robust engineering design involving granular media, and the benefits of improved modeling capabilities are numerous. For example, it is estimated by some that, in industrial plants handling granular materials, 40% of capacity is wasted due to over-design and inefficiencies in equipment and handling procedures [2].

Continuum models, which treat the granular media as a continuous mass rather than considering the individual grains, are the best tools for predicting granular flows in engineering design, as they enable rapid numerical implementation utilizing the finite-element method (FEM). This is in contrast

to grain-by-grain modeling methods, such as the discrete-element method (DEM), which is many times slower than a finite-element method calculation utilizing a continuum model would be. Continuum models are also advantageous due to their generality, as opposed to empirical relations, which are application-specific, relating to specific geometries and conditions.

Despite their pervasiveness, granular materials remain challenging to model from a continuum perspective, and a comprehensive, predictive continuum model remains elusive. Much of this difficulty arises from behavior unique to granular materials, one of which is grain-size dependence. Granular flows of even the simplest variety ultimately depend not only on the geometry of the flow but also on the size of the grains. For example, in a variety of geometries, deforming granular media form clear shear bands – zones of localized flow surrounded by nominally rigid regions [3, 4, 5, 6]. The widths of these shear bands are found to depend not only on the geometry of the flow configuration but also on the grain-size under consideration – a property which is not accounted for by current scale-independent models. Recent work has made progress in incorporating grain-size dependence into a continuum model. The Henann group (under whose auspices this work was carried out) has focused on the development of continuum models that are able to account for grain-size dependence and can predict monodisperse granular flows [7, 8, 9].

In addition to the case of monodisperse mixtures with only one grain-size present, polydisperse systems – systems with multiple grain-size values –

provide a unique set of challenges. Size segregation, a process in which grains of different sizes sort themselves under agitation, is the most important of these [10, 11, 12, 13, 14]. This process is of extreme interest to industry, as mixing materials of different grain sizes is a necessity in many chemical and pharmaceutical applications. The process is present in many natural phenomena as well, being exhibited in landslides and debris flows.

The driving forces of size segregation are twofold: gravity and shear rate. Gravity drives size segregation through a process known as "kinetic sieving" [15], whereby small particles fall downwards through voids between large particles opened by agitation. Shearing flows drive segregation as well [16, 17], with large particles concentrating in regions with a greater shear strain-rate in dense flows. Both forms of segregation are present in many common flow configurations, and so understanding these effects, both in isolation and in combination, is crucial to developing a reliable, robust continuum model of dense granular flow.

The development of a continuum model for the simultaneous prediction of flow and size-segregation in dense bidisperse granular systems is currently the goal of a long-term project funded by NSF grant CBET-1552556, and experimental input is crucial for the purposes of model development and validation. The purpose of this thesis is the creation of robust methods for experimental verification of model predictions for both monodisperse and polydisperse granular systems, focusing on the use of the split-bottom cell geometry. The thesis is organized as follows. In Chapter 2, the split-bottom cell is discussed

in detail. In Chapter 3, we discuss our experimental methodology, and in Chapter 4, results are presented. In Chapter 5, we identify several experimental challenges encountered during this work, and in Chapter 6, we close with conclusions and directions for future research.

Chapter 2

Split-Bottom Cell Background

In this thesis, we use the split-bottom cell flow configuration, originally proposed by van Hecke and co-workers [5], as an experimental platform for studying dense flow of both monodisperse and bidisperse granular systems. This experimental configuration (shown schematically in Fig. 2.1) consists of a rough-walled annular trough with an open top, split in the middle into two sections, the outer of which rotates at an angular velocity Ω. The inner and outer radii of the cell are denoted by R_{i} and R_{o}, respectively, and the radius of the split is R_{s}. The height to which grains are filled is denoted by H. The discontinuity in the floor velocity at the split serves as a nucleation point for a shear band (also shown schematically in Fig. 2.1 with dashed lines).

The split-bottom cell is a flow geometry well-suited to needs of continuum model development. Used by van Hecke and co-workers to study monodisperse flows [5, 18, 19, 20], the split-bottom cell has also been used by Fan

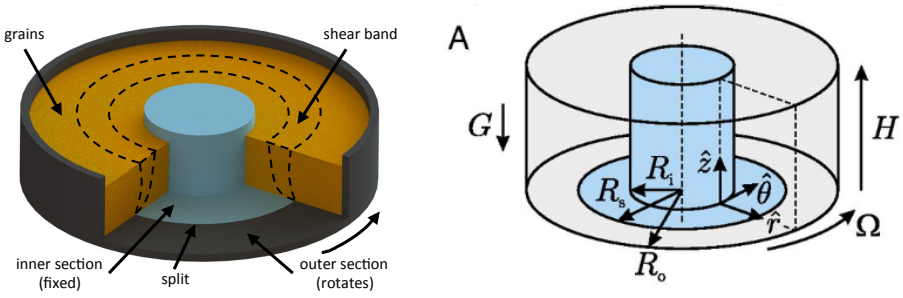

Figure 2.1: A general split-bottom cell, where R_i is the inner cylinder radius (in our case 0), R_s is the split radius, R_o is the outer radius, and H is the filling height. Figure after [21]

and Hill [16, 17] to study both gravitational and shear-driven segregation in a bidisperse system. There are several reasons the split-bottom cell is an ideal choice for testing three-dimensional models for steady granular flow. Firstly, the annular geometry allows for indefinite driving and the elimination of transients. Secondly, wall effects are minimized, since shear bands occur entirely within the bulk. Thirdly, the arrangement contains non-trivial geometries that affect flow, which, via the adjustment of H and R_s, allows for investigation of the effects of geometry. Fourthly, for the case of a bidisperse system, the geometry provides both gravity- and shear-driven size segregation effects. These properties make the split-bottom cell ideal for the study of granular flow.

There are four parameters which are instrumental in determining the resulting flow fields in a split-bottom cell: split radius R_s, filling height H, grain size D, and disk rotation rate Ω. The outer radius does not affect flow fields as long as it is large enough: $\sim$1.25 times as large as R_s seems to be

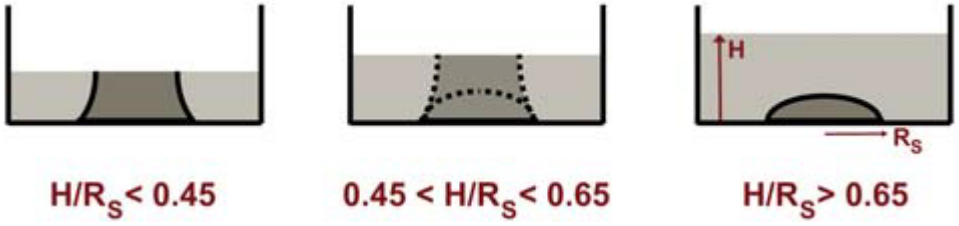

Figure 2.2: Flow regimes in the split-bottom cell. Figure after [20].

adequate [20]. Regarding the inner radius R_i, while Fig. 2.1 features a split-bottom cell with a central cylinder, following the later work of van Hecke and co-workers [19], we will utilize a design without a central cylinder, which eliminates a source of wall effects and irregularities. The split bottom-cell with no inner cylinder has essentially no wall effects, as the flow (a shear band centered on the split radius) is pinned far away from the outer walls.

Qualitatively, the flow generated in a split-bottom cell consists of two approximately static regions with a shear zone between them: the central core driven by the disk, and the outer annular region constrained by the no-slip condition on the outer ring and walls. As can be seen in Fig. 2.2, the shapes of these two regions depends importantly on the geometry of the flow configuration; in particular, the ratio between H and R_s is very important. For shallow layers ($H/R_\mathrm{s} \lesssim 0.45$), the shear band terminates at the free surface as shown in Fig. 2.2(left). As H increases, a gradual transition takes place, leading to a flow characterized by dome-shaped shear band for the case of deep layers ($H/R_\mathrm{s} \gtrsim 0.65$), which is contained entirely within the bulk of the granular media.

For shallow layers, the shear zone, or *shear band* in a split-bottom cell may be experimentally observed from the top surface. To characterize the surface flow field, we introduce the quantity $\omega = v_\theta / r\Omega$, where v_θ is the tangential velocity on the free surface and r is the radial coordinate. The quantity ω is referred to as the normalized revolution rate, which varies from 0 (static) to 1 (rotating at Ω). Importantly, Fenistein, van de Meent, and van Hecke have observed that the dependence of ω on r along the top surface is universal for shallow filling heights and is well-described by an error function. For a given combination of H, R_s, and D, the surface flow field may be described by

$$\omega(r) = 1/2 + 1/2 \ \mathrm{erf}[(r - R_c)/W] \tag{2.1}$$

where R_c is the radial position of the center of the shear band and W is the width of the shear band for the given $\{H, R_\mathrm{s}, D\}$. This leads straightforwardly to a quantitative description of shear band width based on the error function, with the width being between points equivalent to $\mathrm{erf}(\pm\frac{1}{2})$. In what follows, we will focus on shallow layers in a split bottom cell for both monodisperse and bidisperse systems.

Chapter 3

Methodology

3.1 Flow Cell Apparatus

Several key parameters define a split-bottom flow - split radius R_s, filling height H, rotation rate ω, and grain size D. In this project, a split-bottom cell was constructed with an outer radius of $R_o = 98.425$mm and a split radius $R_s = 60.325$mm. The cell was composed of a polycarbonate cylinder attached to a base constructed out of aluminum framing and Delrin. The split-bottom disk was driven by a gearmotor with an attached encoder, allowing for control and measurement of rotation rate ω. Control and data acquisition for the motor was handled by an Arduino connected to a control computer.[1]

The granular materials used in this experiment were glass beads produced by Jaygo, Inc. Two sizes were investigated: 1.55mm and 0.75mm. The

[1]The design of the split-bottom cell was completed as part of a capstone design project, and the final project report is included in appendix A.

0.75mm beads were only used for the bidisperse system investigations. The filling height H was determined by probing the grains in the cell vertically with a small thin rod marked at the measured height.

3.2 Data Capture and Analysis

3.2.1 Monodisperse System

A Nikon D7100 was used to capture video of the top free surface of the flow cell at a certain filling height once a steady state flow had developed, resulting in the field of view seen in figure 3.1. Data was gathered for values of $\frac{H}{R_s} = \{0.2, 0.4, 0.6\}$, with an applied angular velocity of $0.53\text{rad}\,\text{s}^{-1}$. The flow surface was illuminated with two LED light panels, which were used without diffusers to provide high-contrast bright spots on each particle. Each run was recorded for half an hour, and the resulting video was cropped using the Handbrake video processing tool to isolate a region of flow away from the highly-saturated and over-exposed cells walls, the result of which can be seen in figure 3.2. The video was also time-cropped to remove periods of shaking (originating from camera manipulation) at the beginning and end of the video. The video was then then passed to a modified version of the FIDIC MATLAB program[23]. This program takes a series of images and uses digital image correlation (DIC) methods to generate a displacement field for each consecutive pair of images. For this project, FIDIC was run on the entire video, and the displacement fields were time-averaged to produce

Figure 3.1: Full field of view

average velocity fields for the field of view.

To arrive at a description of the flow velocity as a function of radius, the flow velocity was plotted as a function of radius. In order to generate this data, the center of the flow was found by finding the point of minimum velocity. The polar coordinates of each data point were computed in reference to this center, and the velocities were converted from Cartesian to polar form. This allowed for the plotting of the tangential velocity u_θ as a function of radius. In most of the cases, radial velocity was approximately zero, as radial flow is minimal in the split-bottom configuration, allowing for easier computation of the total velocity vector.

Figure 3.2: Cropped field of view

3.2.2 Bidisperse System

In the bidisperse case, a mixture of two sizes of particles was made using equal volumes of each particle. These were mixed by pouring them into a sealed container and inverting several times. The mixture was then poured into the cell and leveled. The camera was then used to capture video of the flow surface, starting from rest, and the system was recorded for approximately 10 minutes. This was enough time to allow size segregation to occur and for clear bands of large grains to form on the surface. The images were then processed, via thresholding, to extract the points of light on the beads originating from the light panel. These were created by first trimming the image to the circle of the cell, thresholding the image aggresively, and using the MATLAB `regionprops`function to extract the locations of each bright

Figure 3.3: Large and small beads

spot, each of which is centered on a bead. This process can be seen in figure 3.4. For each spot, the sum of the inverse square distance to every other point was summed, giving a value for density. The density of these points was used as a proxy for large grain density – as can be seen in figure 3.3, bright spots on large beads are necessarily farther away from their neighbors than those on small beads. While identification of individual beads would be preferable, for various reasons, the large and small beads used in this project were the same color, making distinguishing between them very difficult.
The density data was then plotted as a function of radius, thus giving a proxy for large grain density. The density levels at the center of the band when well-developed, as well as the average density level at the initial time,

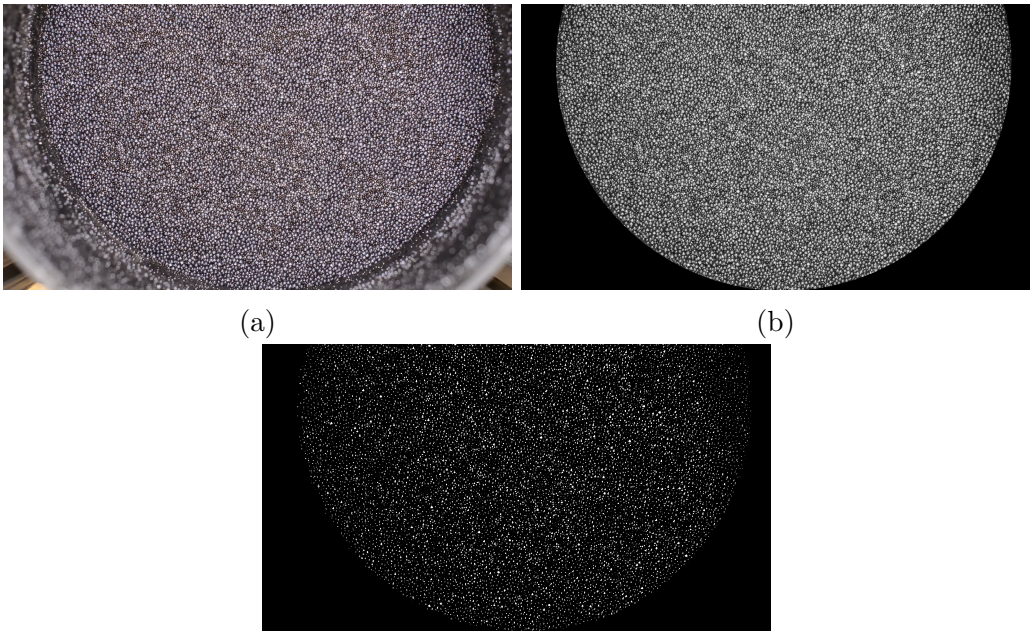

(a) (b)

(c)

Figure 3.4: An image of the bidisperse system (a) in full, (b) trimmed, and (c) thresholded.

were used to give reference values for large grain concentration of 1 and 0.5 respectively.

Chapter 4

Results and Discussion

4.1 Monodisperse System

The velocity data acquired in the monodisperse trials can be seen in figure 4.1. In all results in this section, ω represents the angular velocity from DIC normalized by the applied angular velocity. The data were fit with an error function according to the method used by Fenistein, van de Meent, and van Hecke[22], and were renormalized according to shear band width. When normalized in this way, it can be seen that the profiles for different filling heights collapse to a single curve, given by equation 2.1, as seen in figure 4.2. The data is fit relatively closely, and as can be seen in figure 4.3, the decay of the data matches the fit closely, down to the noise floor of 10^{-5}. In addition, the three studies conducted conform to the power-law relations for W, H, and R_c below, as described by Fenistein, van de Meent, and van Hecke for

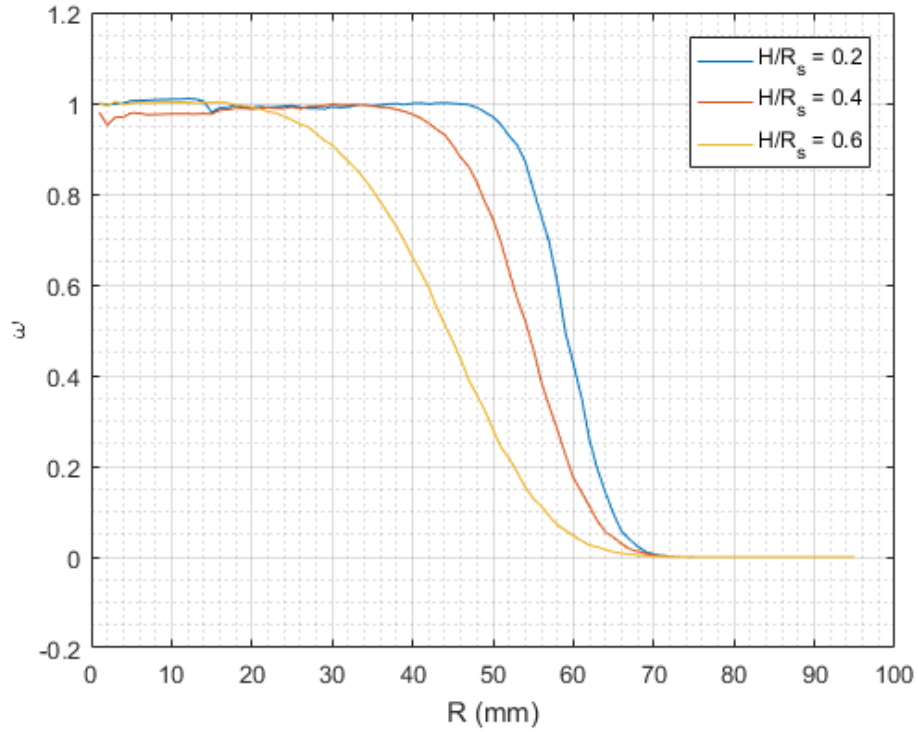

Figure 4.1: Velocity data at three filling heights

the split-bottom cell.

$$\frac{R_s - R_c}{R_s} = \left(\frac{H}{R_s}\right)^{5/2} \tag{4.1}$$

$$\frac{W}{D} \sim \left(\frac{H}{D}\right)^{\frac{2}{3}} \tag{4.2}$$

As can be seen in figures 4.4 and 4.5 respectively, the data match the power laws very closely.

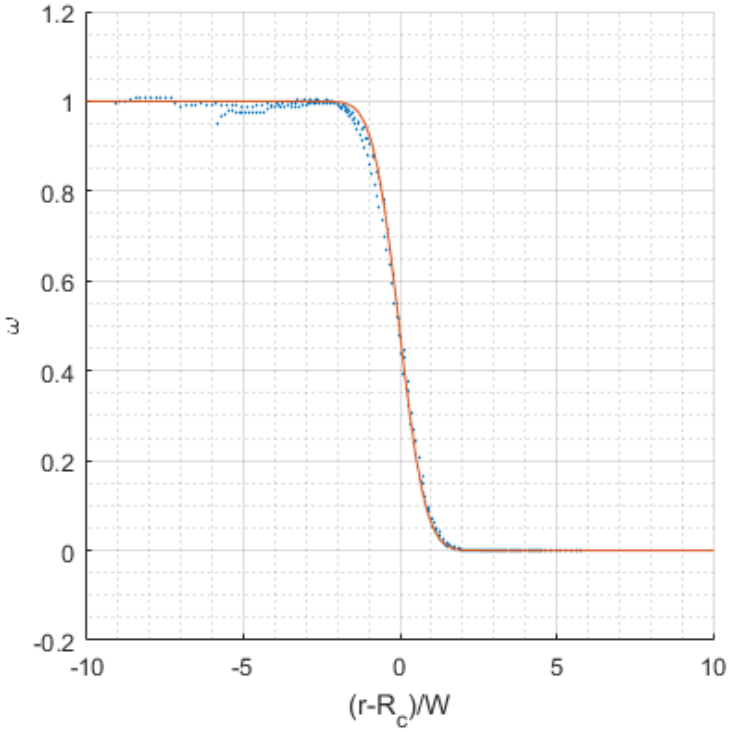

Figure 4.2: Renormalized data from Fig. 4.1

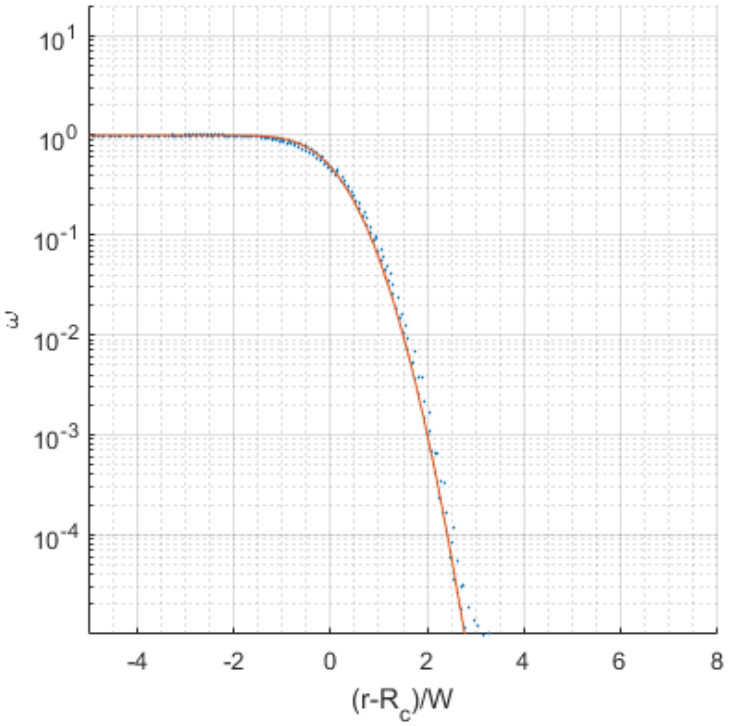

Figure 4.3: Semilog plot showing velocity decay

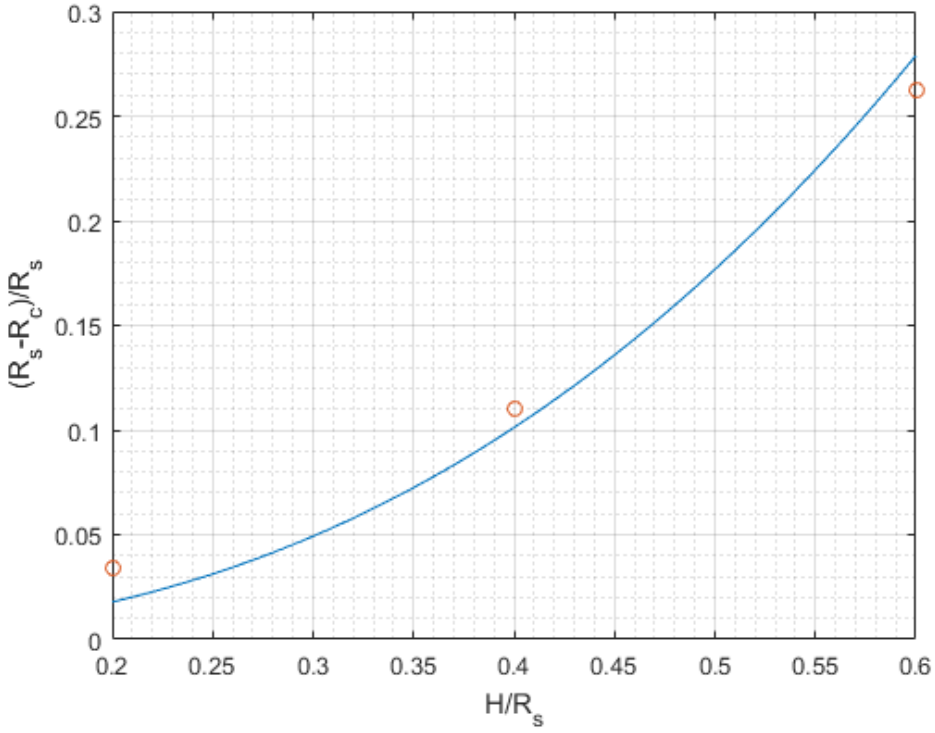

Figure 4.4: Relation between shear band center position R_c and filling height H. Solid line is Eq. 4.1.

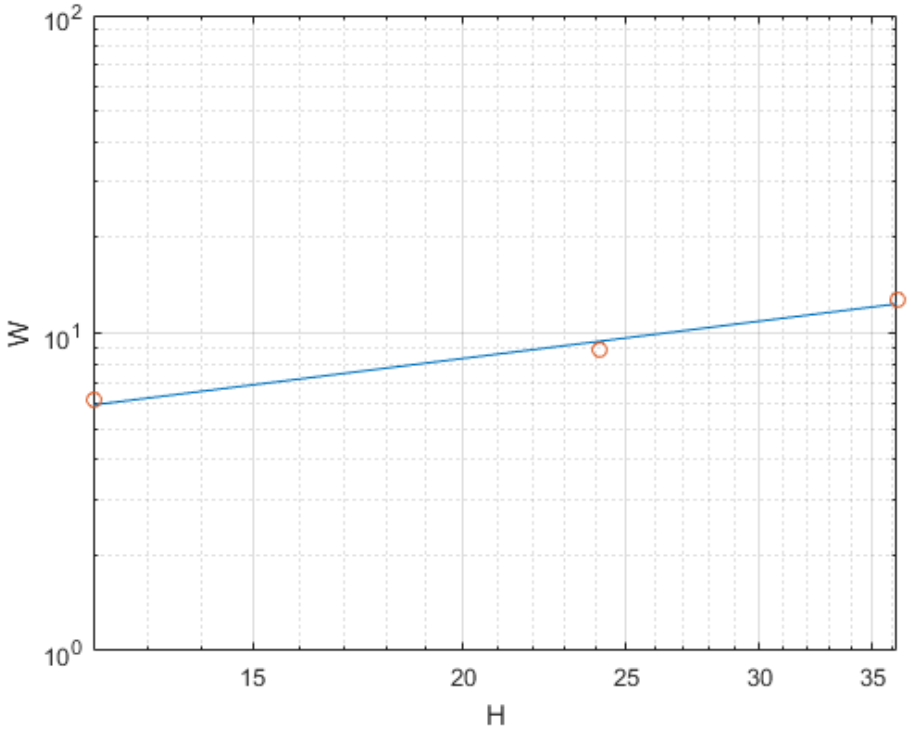

Figure 4.5: Relation between shear band width and filling height H. Solid line is Eq. 4.2.

4.2 Bidisperse System

For the bidisperse case, the data consist of density maps for frames of video. As can be seen in figs. 4.6 to 4.11, the surface of the flow develops a banded structure that is clearly visible in the density plots. The density was then plotted with respect to radius. The results can be seen in figs. 4.6 to 4.11. As time passes, a segregation band develops, initially forming as a relatively small perturbation to the large grain fraction, but over time developing into a wide band that expands continuously as the system is driven. Compare, for example, figures 4.8 and 4.11: the density peak is much higher and broader at large times, which is consistent with observations from the literature[17]. The effect develops quickly; there is a noticeable difference between figure 4.6 and figure 4.7. In the former, the system is completely at rest, and it can be taken as an initial condition. In the latter, however, despite being recorded under a second after the system began moving, the shape of the density function has already changed, and a peak has begun to form.

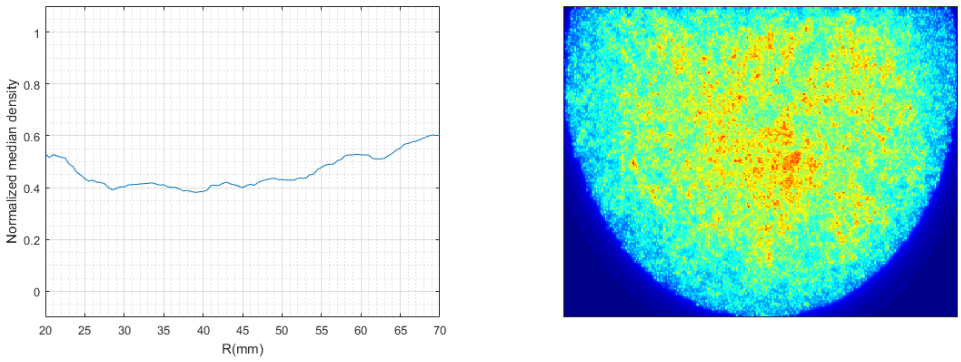

(a) (b)

Figure 4.6: Density plot (a) and map (b) at $\theta = 0$rad

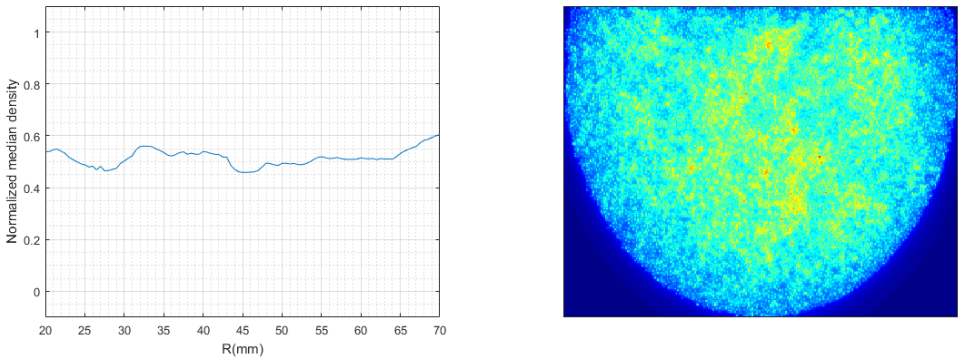

(a) (b)

Figure 4.7: Density plot (a) and map (b) at $\theta = 0.6$rad

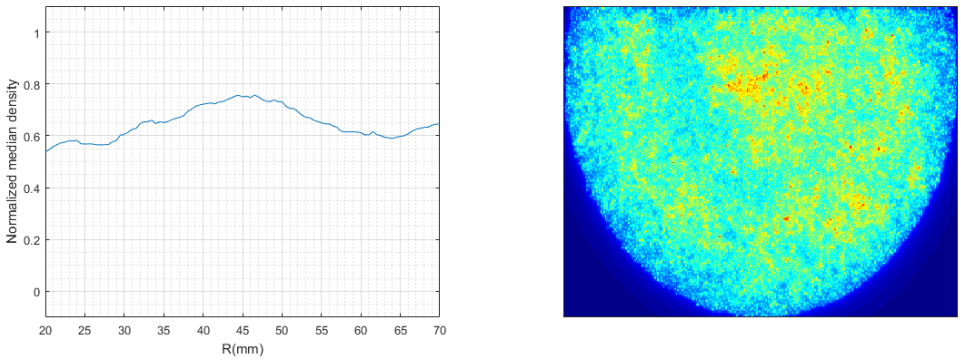

(a) (b)

Figure 4.8: Density plot (a) and map (b) at $\theta = 3.1$rad

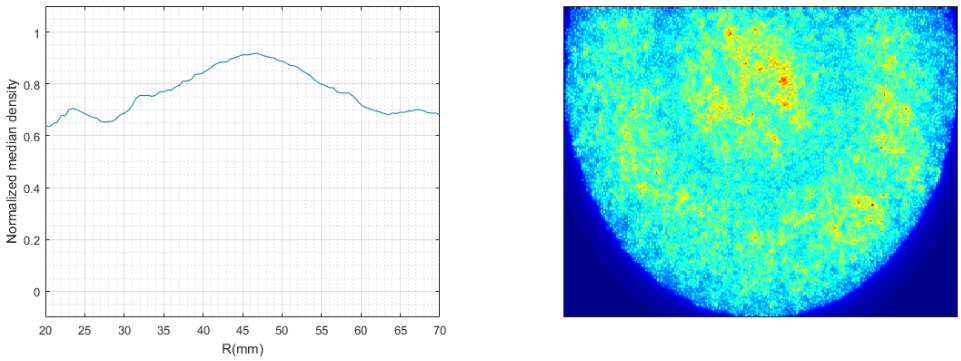

(a) (b)

Figure 4.9: Density plot (a) and map (b) at $\theta = 5.9$rad

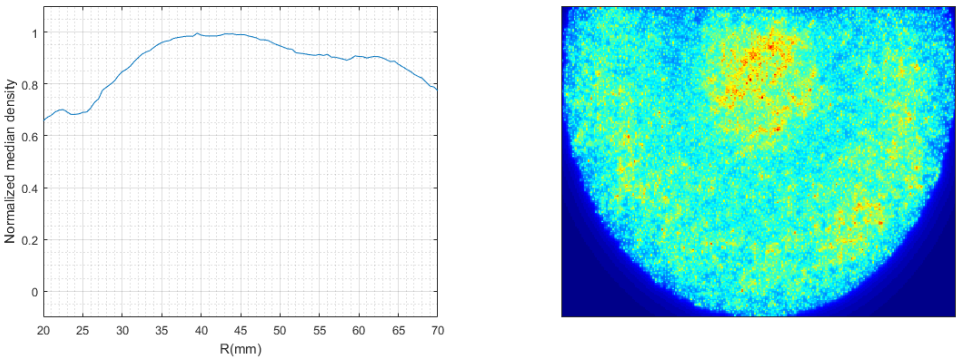

(a) (b)

Figure 4.10: Density plot (a) and map (b) at $\theta = 53.6$rad

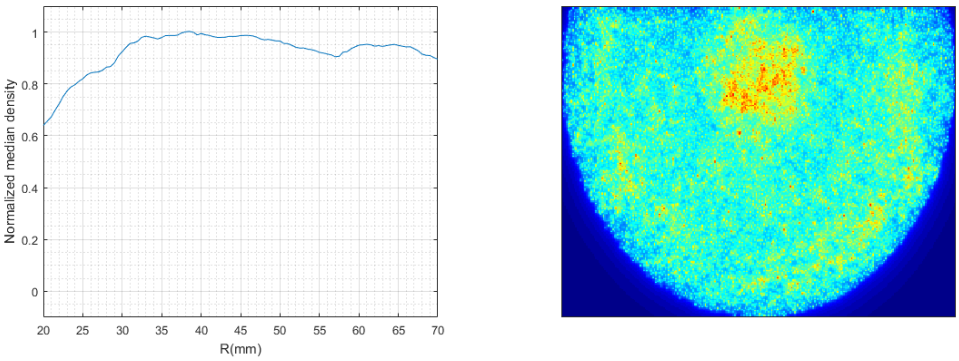

(a) (b)

Figure 4.11: Density plot (a) and map (b) at $\theta = 276.1$rad

Chapter 5

Experimental Challenges

The results of this project point towards a robust method for monodisperse flow characterization, but more work is still needed to develop a similarly reliable method for the study of bidisperse flow systems. The difficulty of distinguishing individual grains in the bidisperse system would be easily remedied by the use of different colors of grains; black and white would allow the use of existing grains, but using different colors of grains (red and blue, etc.) could allow for even easier distinction of grain size ratios. This would allow for the use of simpler methods (e.g., computing the fraction of pixels exhibiting a certain color range) that would simultaneously give more robust and repeatable results.

The flow cell itself is a mostly robust piece of apparatus, with the ability to be reconfigured for multiple split radii and filling heights. Perhaps the biggest issue with the device as it is currently is the inability to run the cell

at very low speeds. As it currently operates, the cell can run as slow as around 0.5 $\mathrm{rad\,s^{-1}}$ before stopping due to the lower power developed at such lower rates. A better choice would be a stepper motor, which would allow for precise control of speed without worrying about encoders. Stepper motors have higher torque, and would allow for better repeatability in experiments. Slower rates would also make it easier to record data - higher speeds require video to obtain images with a low-enough level of displacement to allow for FIDIC, which then makes the data very difficult to work with, as video is a difficult data format to use in a parallelized program. Lower speeds would enable the usage of photos, which would have a higher resolution, better control over focus and lighting, and perhaps most importantly, would enable full parallelization of the image processing tasks.

The flow cell was filled to various values of $\frac{H}{R_s}$ for different trials. H was known to within one grain diameter of the prescribed filling height due to the method of filling. This is a possible source of error, but given the low granularity of the values of H used, the impact is proportionally small. However, this parameter could be better controlled in the future, and alternative methods of filling could be used to better control this important parameter.

Finally, one of the primary difficulties encountered when working with bidisperse systems is the phenomenon of size segregation itself. While the mixing methods used in this project (repeated inversion in a sealed container) work well enough, it is very difficult to evenly tamp down the surface to form a flat free surface. More work is necessary to develop a method for flattening

that minimally disturbs the surface.

Chapter 6

Conclusions and Future Work

This project successfully developed a system for obtaining reliable surface velocity measurements, and the data collected are in agreement with the literature. Monodisperse system data collected exhibited clear velocity profiles that match very well with data reported by other workers[22]. This system will likely be more than adequate for verification of model results for monodisperse systems. While bidisperse system data was not of the same form as that in the literature[17], the large-scale trends exhibited by the data match up well to other sources. The density plotting method works decently well for viewing trends, but a better method, such as multi-colored beads, might work better and be faster. Future work would likely be able to remedy many of the issues faced by this experiment, with many of the changes proposed above resulting in speed-ups due to computational parallelization and more direct measurement of properties.

Bibliography

[1] P. Richard. “Slow relaxation and compaction of granular systems”. In: *Nat. Mater.* 4 (2005), pp. 121–128.

[2] B. J. Ennis, J. Green, and R. Davies. “The legacy of neglect in the US”. In: *Chem. Eng. Prog.* 90 (1994), pp. 32–43.

[3] D. M. Mueth, H. M. Jaeger, and S. R. Nagel. “Force distribution in a granular medium”. In: *Phys. Rev. E* 57 (1998), pp. 3164–3169.

[4] W. Losert et al. “Particle dynamics in sheared granular matter”. In: *Phys. Rev. Lett.* 85 (2000), pp. 1428–1431.

[5] D. Fenistein and M. van Hecke. “Wide shear zones in granular bulk flow”. In: *Nature* 425 (2003), p. 256.

[6] G. D. R. Midi. “On dense granular flows”. In: *Euro. Phys. Journ. E.* 14 (2004), pp. 341–365.

[7] K. Kamrin and G. Koval. “Nonlocal Constitutive Relation for Steady Granular Flow”. In: *Phys. Rev. Lett.* 108 (17 2012), p. 178301.

[8] D. L. Henann and K. Kamrin. “A predictive, size-dependent continuum model for dense granular flows”. In: *P. Natl. Acad. Sci. USA* 110 (2013), pp. 6730–6735.

[9] D. L. Henann and K. Kamrin. “Continuum thermomechanics of the nonlocal granular rheology”. In: *Int. J. Plasticity* 60 (2014), pp. 145–162.

[10] G. Metcalfe et al. “Avalanche mixing of granular solids”. In: *Nature* 374 (1995), pp. 39–41.

[11] J. J. McCarchy et al. “Mixing of granular materials in slowly rotated containers”. In: *AIChE J.* 42 (1996), pp. 3351–3363.

[12] H. A. Makse et al. “Spontaneous stratification in granular mixtures”. In: *Nature* 386 (1997), pp. 379–382.

[13] J. M. N. T. Gray and K. Hutter. “Pattern formation in granular avalanches”. In: *Continuum Mech. Thermodyn.* 9 (1997), pp. 341–345.

[14] T. Shinbrot and F. J. Muzzio. “Nonequilibrium patterns in granular mixing and segregation”. In: *Physics Today* 53 (2000), p. 25.

[15] S. B. Savage and C. K. K. Lun. “Particle size segregation in inclined chute flow of dry cohesionless granular solids”. In: *J. Fluid Mech.* 189 (1988), pp. 311–335.

[16] K. M. Hill and Y. Fan. “Isolating Segregation Mechanisms in a Split-Bottom Cell”. In: *Phys. Rev. Lett.* 101 (2008), p. 088001.

[17] Y. Fan and K. M. Hill. "Shear-driven segregation of dense granular mixtures in a split-bottom cell". In: *Phys. Rev. E* 81 (2010), p. 041303.

[18] D. Fenistein, J. W. van de Meent, and M. van Hecke. "Universal and Wide Shear Zones in Granular Bulk Flow". In: *Phys. Rev. Lett.* 92 (2004), p. 094301.

[19] D. Fenistein, J. W. van de Meent, and M. van Hecke. "Core Precession and Global Modes in Granular Bulk Flow". In: *Phys. Rev. Lett.* 96 (2006), p. 118001.

[20] Joshua A. Dijksman and Martin van Hecke. "Granular flows in split-bottom geometries". In: *Soft Matter* 6 (2010), pp. 2901–2907. DOI: 10.1039/b925110c.

[21] David L. Henann and Ken Kamrin. "A predictive, size-dependent continuum model for dense granular flows". In: *Proceedings of the National Academy of Sciences of the United States of America* 110.17 (2013), pp. 6730–6735.

[22] Denis Fenistein, Jan Willem van de Meent, and Martin van Hecke. "Universal and Wide Shear Zones in Granular Bulk Flow". In: *Phys. Rev. Lett.* 92 (9 Mar. 2004), p. 094301. DOI: 10.1103/PhysRevLett.92.094301.

[23] E. Bar-Kochba et al. "A Fast Iterative Digital Volume Correlation Algorithm for Large Deformations". In: *Experimental Mechanics* 55.1 (2015), pp. 261–274. DOI: 10.1007/s11340-014-9874-2.

[24] J. A. Dijksman and M. van Hecke. “Granular flows in split-bottom geometries”. In: *Soft Matter* 6 (2010), pp. 2901–2907.

Appendices

Appendix A

Bidisperse System Raw Density Data

The data presented in section 4.2 was filtered from the form presented below; while the density data derived via the sum of inverse square distances is noisy, the trends seen in the median filtered data above are clearly reflected in the unfiltered data below. While this method has produced relatively clear results, we hope to use a more robust method of grain size discrimination in the future.

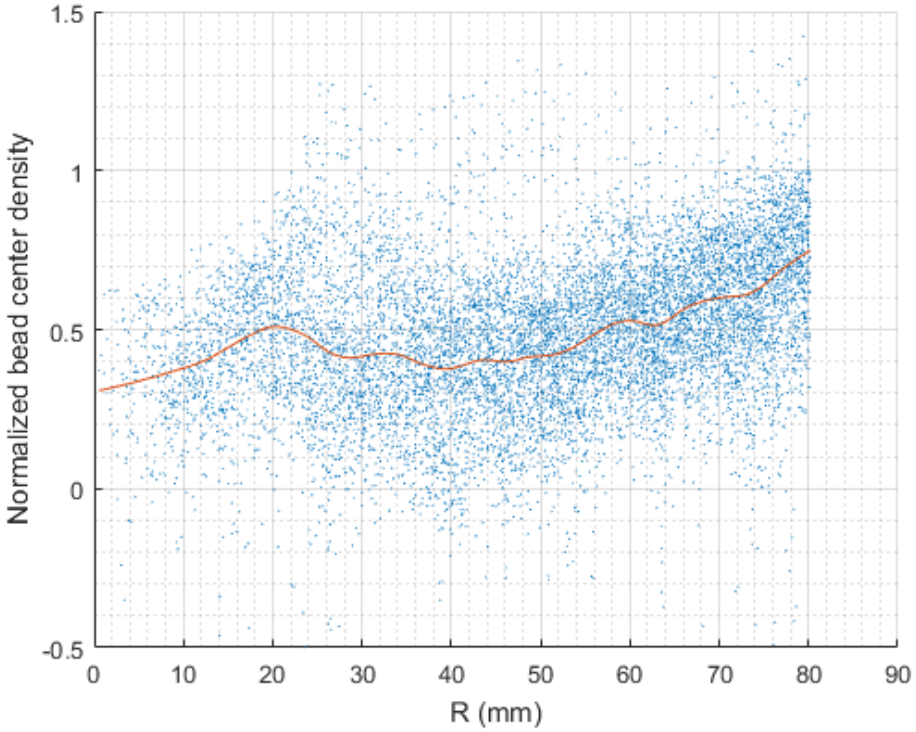

Figure A.1: $\theta = 0$rad

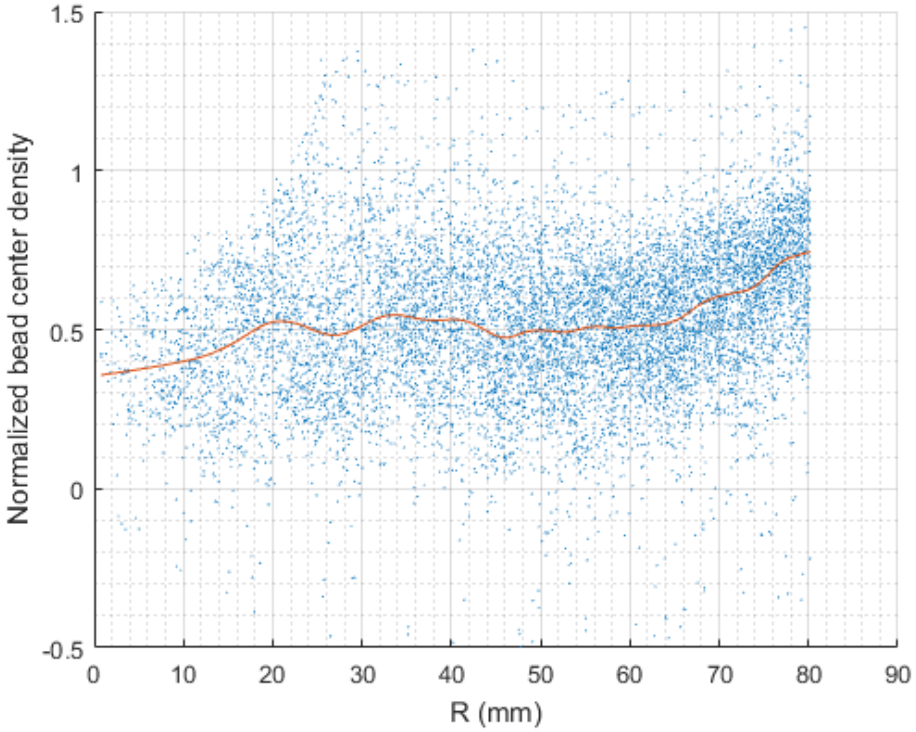

Figure A.2: $\theta = 0.6$rad

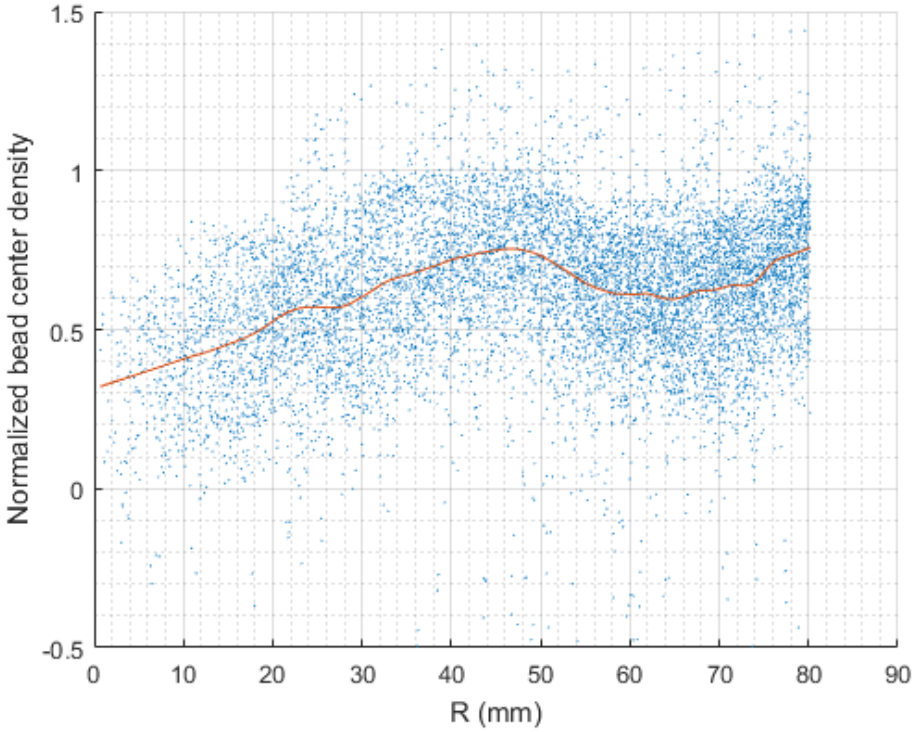

Figure A.3: $\theta = 3.1$rad

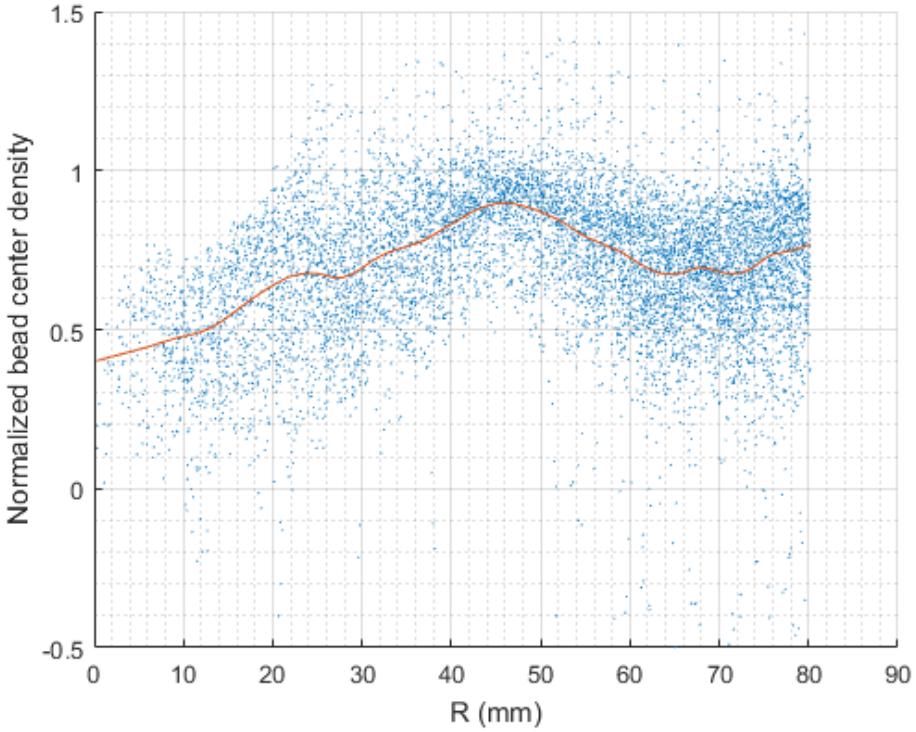

Figure A.4: $\theta = 5.9$rad

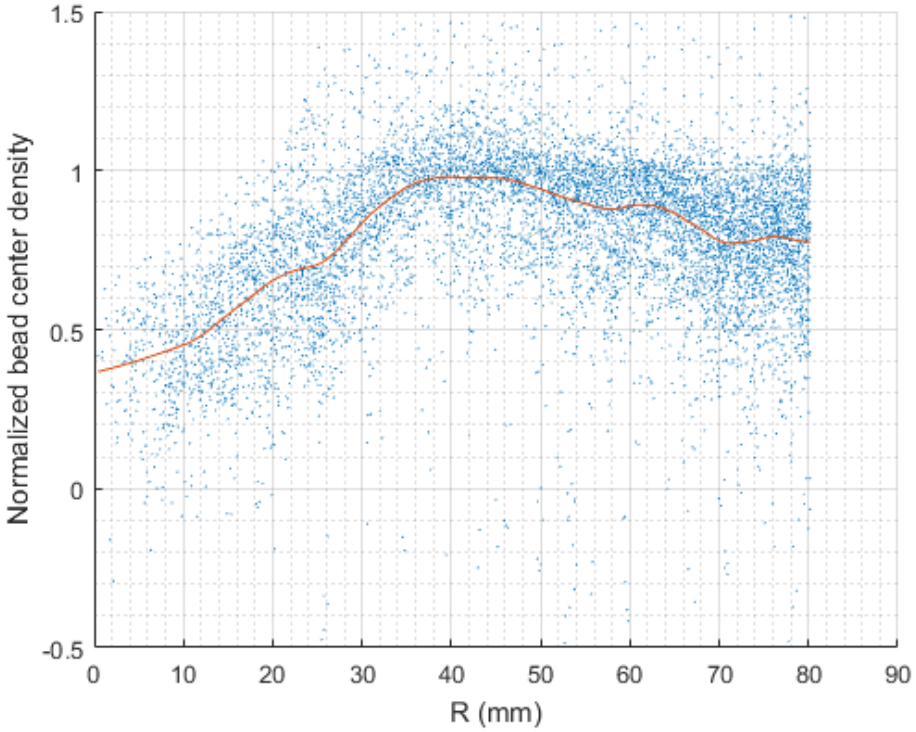

Figure A.5: $\theta = 53.6$rad

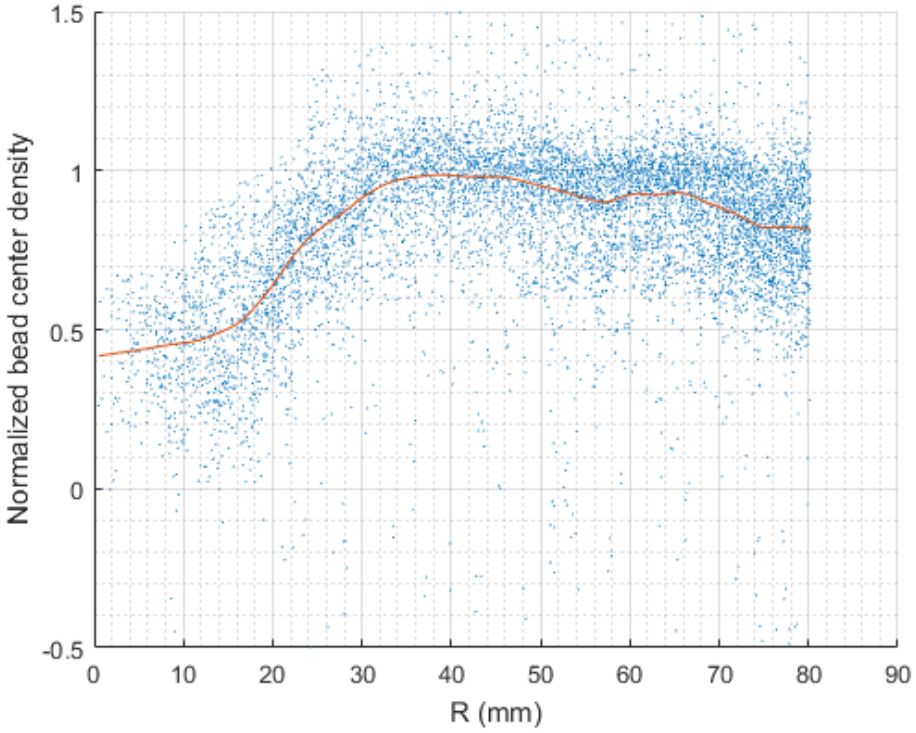

Figure A.6: $\theta = 276.1$rad

Appendix B

Development of a Split-Bottom Cell for Granular Flow Experiments[1]

The split bottom cell (SBC) is a useful geometry for the study of granular flows. Introduced by Fenistein and Hecke[5], the SBC originally comprised an annular Couette cell with a split bottom at a split radius R_s. Either the interior wall and inner bottom annulus or the exterior wall and out bottom annulus can be driven. The SBC is useful because it allows for the generation of steady-state and transient flows with relative ease, and can be run indefinitely due to its rotational nature. More detail on the features of the SBC

[1]The work in this appendix was carried out as part of a senior-level engineering design capstone project. This appendix, in report form, was submitted as the deliverable for that capstone requirement.

can be found in a review article by Dijksman and Hecke[24]. The SBC is primarily of interest as a reference geometry for the development and validation of continuum models of granular flow.

B.1 Experimental Considerations

The flow geometry has several useful properties: the shear bands created by the SBC are pinned away from the walls by the split. As walls can introduce unwanted boundary effects that can contaminate collected data, this increases the quality of data collected. The geometry also lends itself to the study of steady-state flows due to the its rotational nature, which enables long-term driving at constant rates. The project this flow cell was constructed for focused on collecting photo and video of the top surface of the flow for analysis using digital image correlation methods.

This particular split-bottom cell was constrained by several concerns relating to experimentation:

- the rotation rate needed to be controlled to within a tenth of a radian per second,
- the top of the cell needed to be open to allow for visual recording of the top surface, and
- the cell needed to be illuminated to allow for optimal recording conditions.

The cell apparatus therefore comprises several components: the cell itself, with an attendant control system; the lighting system, to illuminate the surface of the flow; and a camera system, to collect data.

B.2 Design

The design of the flow cell itself was carried out in Autodesk Inventor. Drawings were created, which are seen below. The construction of the initial version of the flow cell was carried out by Anna Seto over the summer of 2015. The flow cell was driven by an AndyMark PG-71 high-torque gearbox with an RS775 motor, controlled by a Parallax HB-25 motor controller. The power supply was an off-the-shelf 12V switched power supply, and the motor was to be controlled using a National Instruments USB-6501 DAQ and LabView running on a PC.

Mechanically, the original device design consisted of a polycarbonate cylinder (OD 8 in, thickness 0.125 inches) inserted into a Delrin base as seen in figure B.1. A hole in the Delrin base allowed for an adapter, seen in figure B.2, to go between the motor output shaft and the driven disk. The motor itself was attached to the assembly with the bracket seen in figure B.4.

The driven disk formed a set with the outer ring, with the split between them defining the set. Different sets were made, and they were straightforward to cut out of plastic sheet (various materials, 0.25 inch thickness) on a laser cutter. These sets, and the interior wall of the cell, were coated with

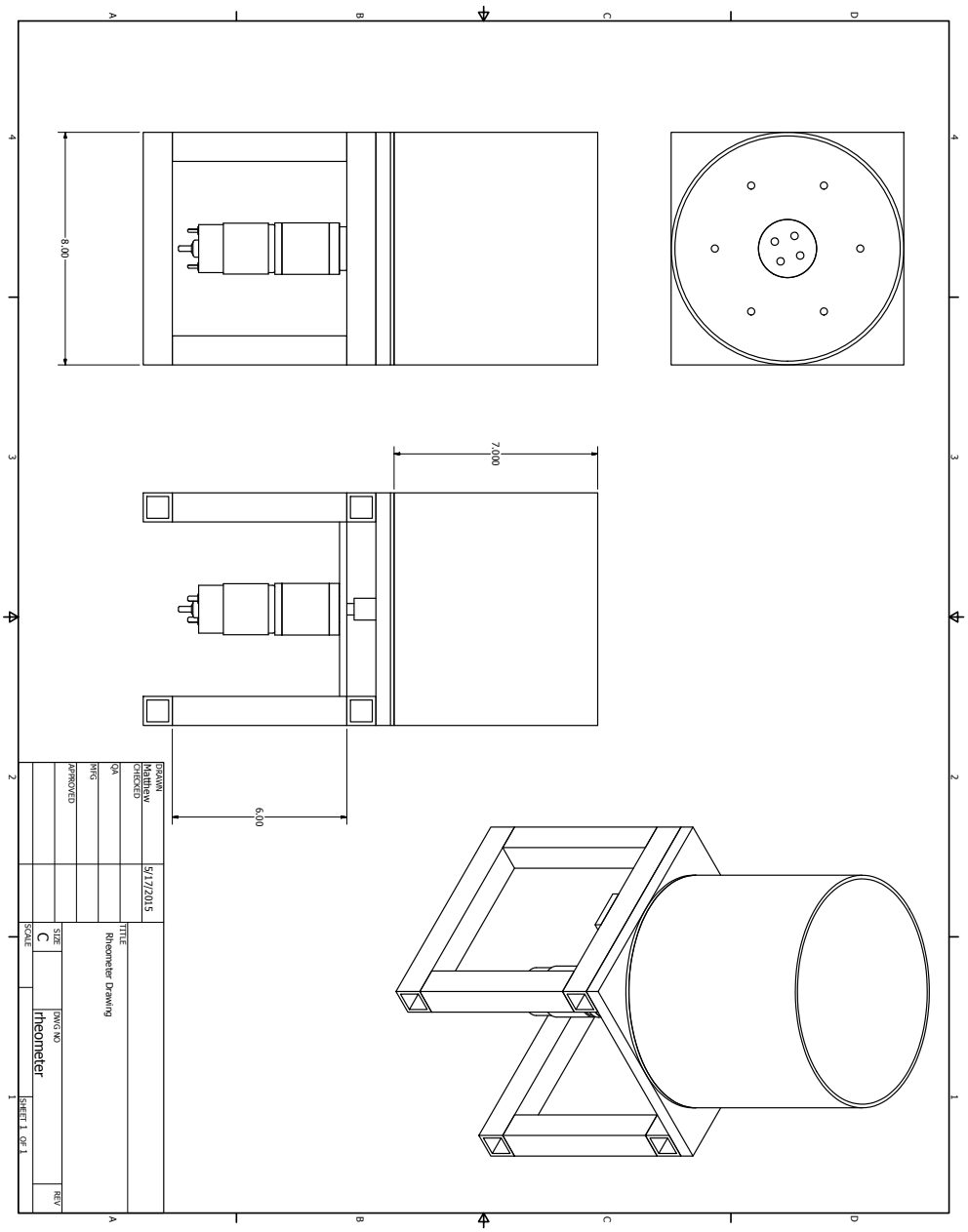

Figure B.1: Flow cell Assembly

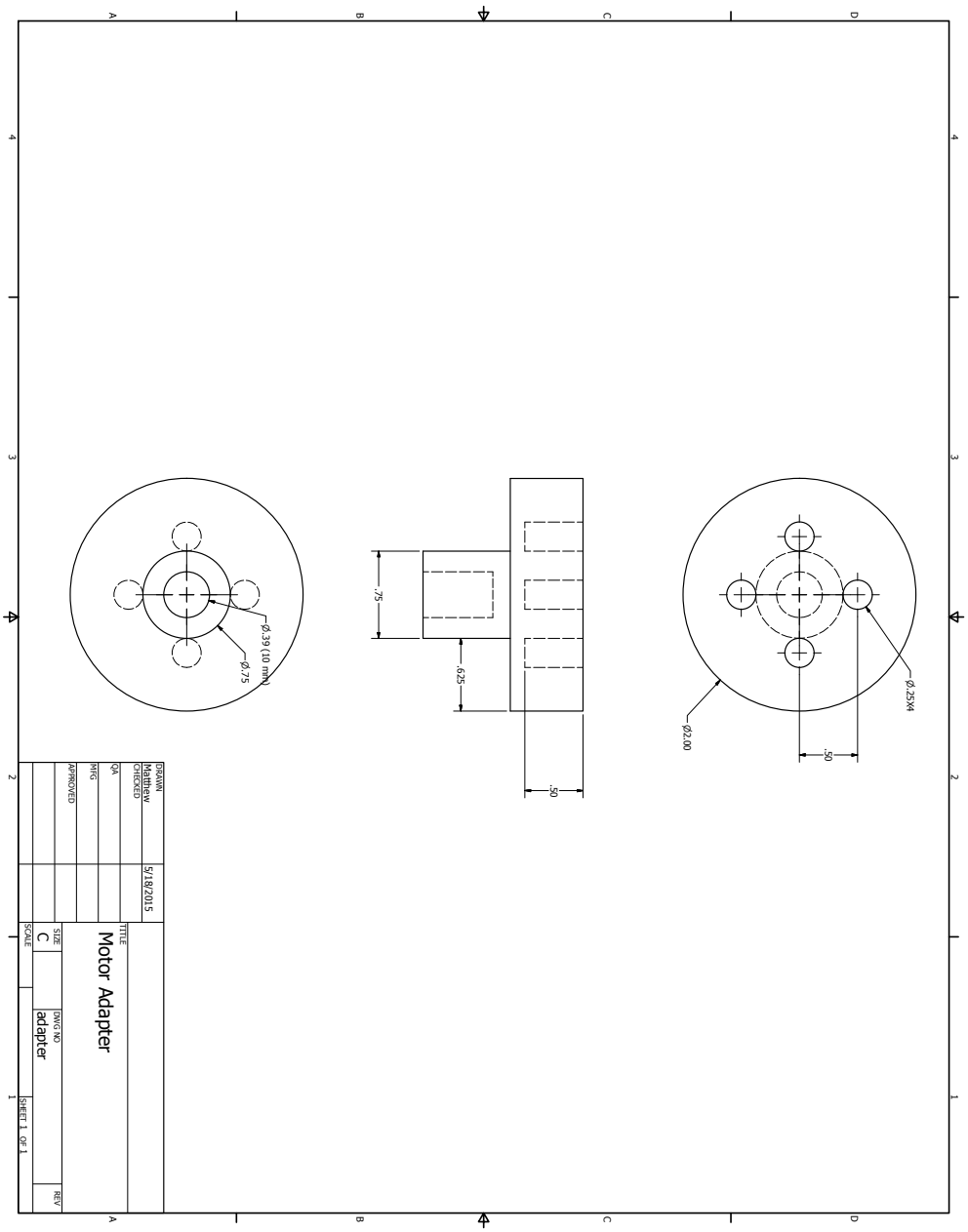

Figure B.2: Motor adapter

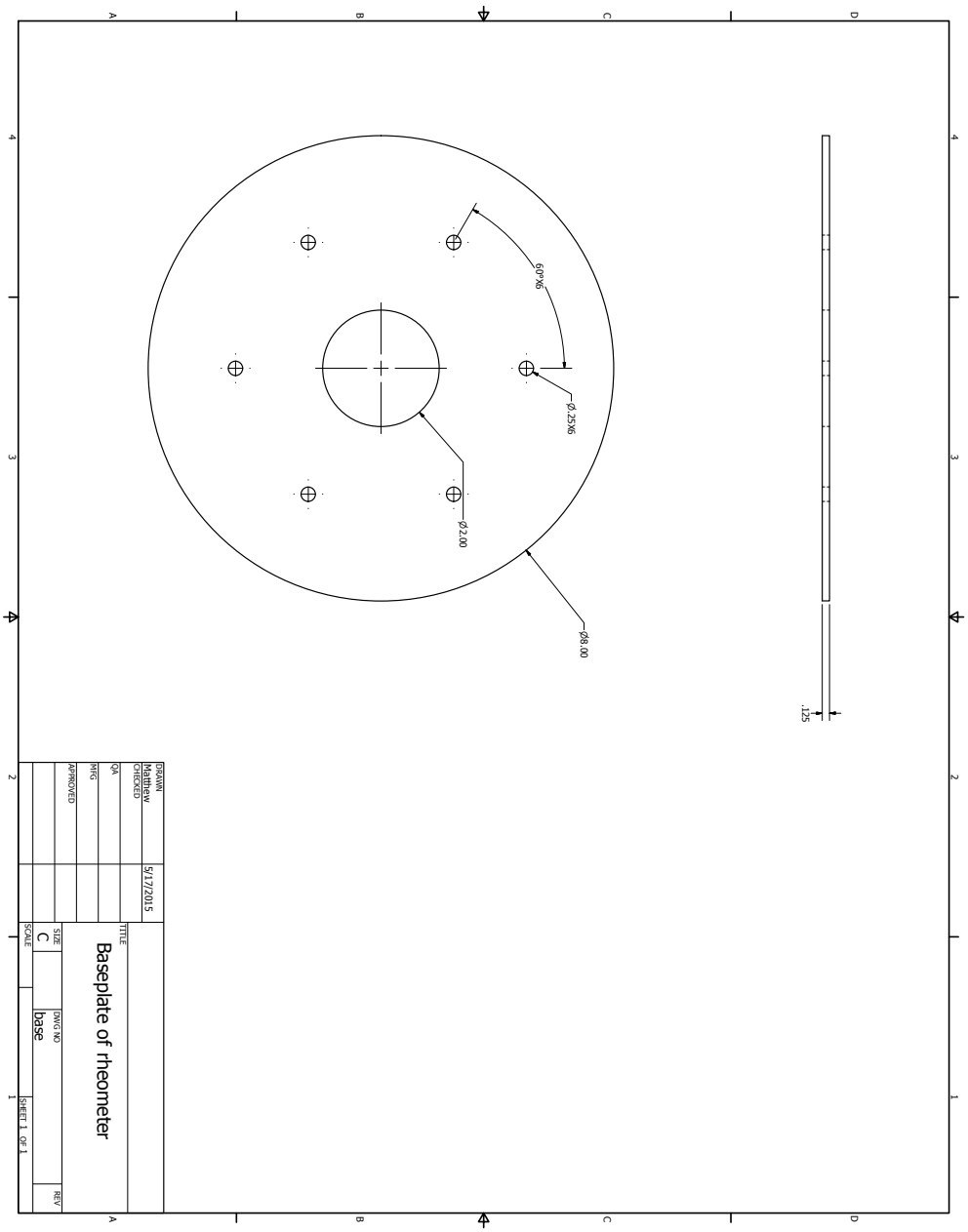

Figure B.3: Flow cell base hole pattern

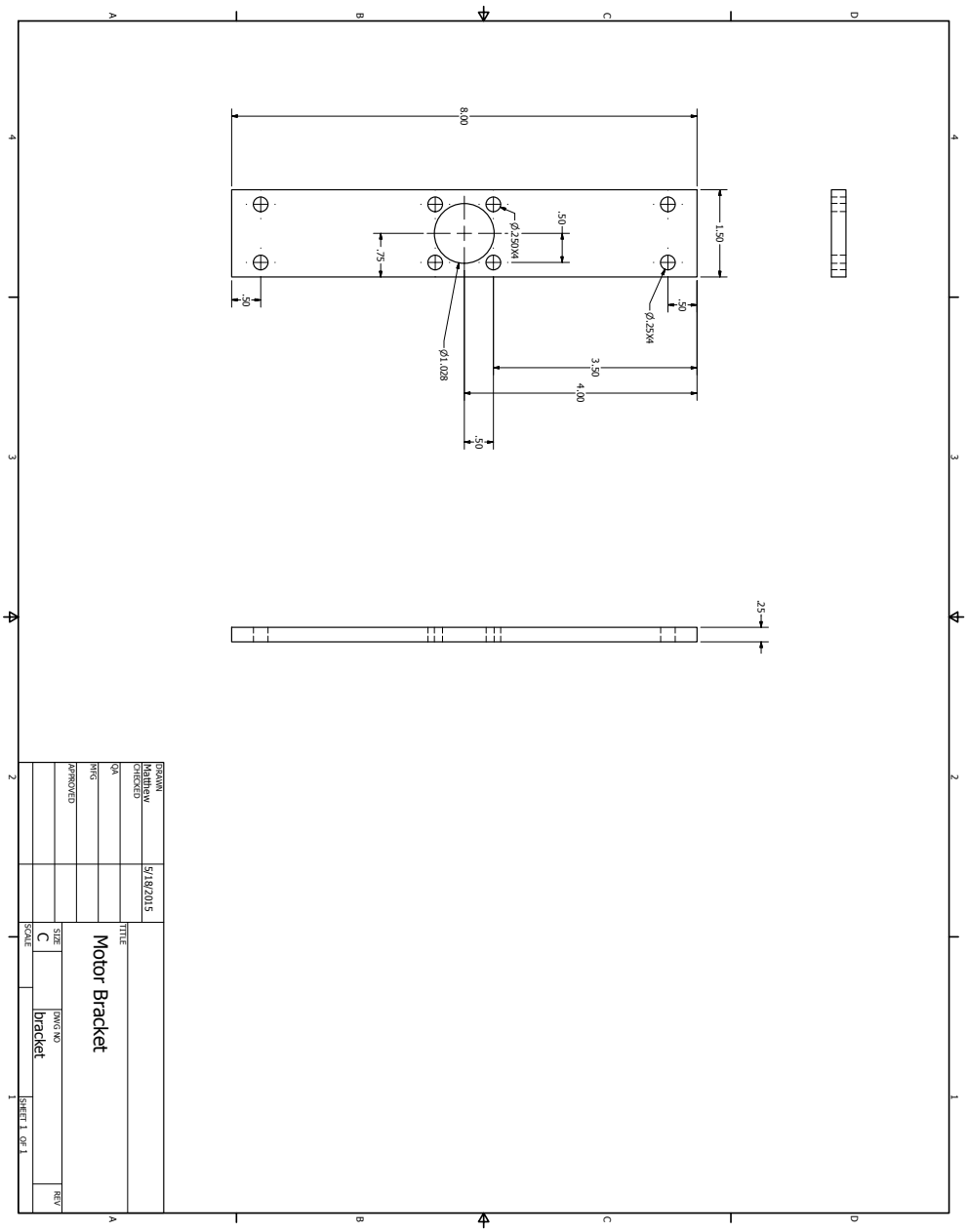

Figure B.4: Motor bracket

1.55mm diameter glass grains, the larger size of grain being investigated. The larger size of grain was chosen due to it's ability to impose a no-slip condition at the wall and base for both large and small grains.

The disk and ring sets were affixed to the motor adapter and the flow cell base by using a set of steel dowel pins embedded in the adapter and base. These pins, in the patterns seen in figs. B.2 and B.3, mate with matching divots in the disk and ring.

B.3 Iteration

Upon use of the device this year, several flaws became evident. First of all, the motor controller system was found to be too difficult to use, with LabView proving difficult to integrate with the encoder mounted on the motor. In addition, the DAQ unit was simply overkill, and better suited to larger-scale laboratory setup or small-scale industrial automation. As a replacement, an Arduino microcontroller was used to serve as the main controller, making use of existing encoder and motor controller libraries to help with development. A simple serial console interface was used to control the system, and calibration with a digital tachometer was used to convert encoder counting rates to $\mathrm{rad\,s^{-1}}$.

The second issue with the system was lighting. The initial design did not include specifications for lighting or camera concerns. I consulted with Alexander Landauer in the Franck Group to learn about the concerns that

motivate light and camera placement. For this project, the image data was to be used for displacement measuring using the FIDIC protocol developed by the Franck Lab. This protocol benefits from clearly defined speckle patterns that undergo continuous deformation between frames. Therefore, we eventually chose to use a high angle of illumination, with a camera positioned pointing vertically down at a similar position. This configuration results in a high-contrast image, with bright spots on the top of the grains. The system was illuminated using a Genaray SP-E-240D LED light panel, and recorded with a Nikon D7100 DSLR. This configuration was used for the bidisperse system recordings, and a very similar arrangement, but with two light panels, was used for the monodisperse system recordings.

B.4 Future Work

Overall, this system worked fairly well for the monodisperse case, and the difficulties with the bidisperse case, while considerable, stemmed from grain choice rather than the flow cell itself. However, one key issue with the design was the choice of motor. The motor used, while powerful at higher speeds, develops a very low torque at the low speeds required. This mismatch originated in a poor initial understanding of the requirements, and while the speed was sufficiently slow to perform the required analysis, a slower speed would allow for photographs to be used instead of video, enabling parallelized data processing instead of the current video-based non-parallelizable processing

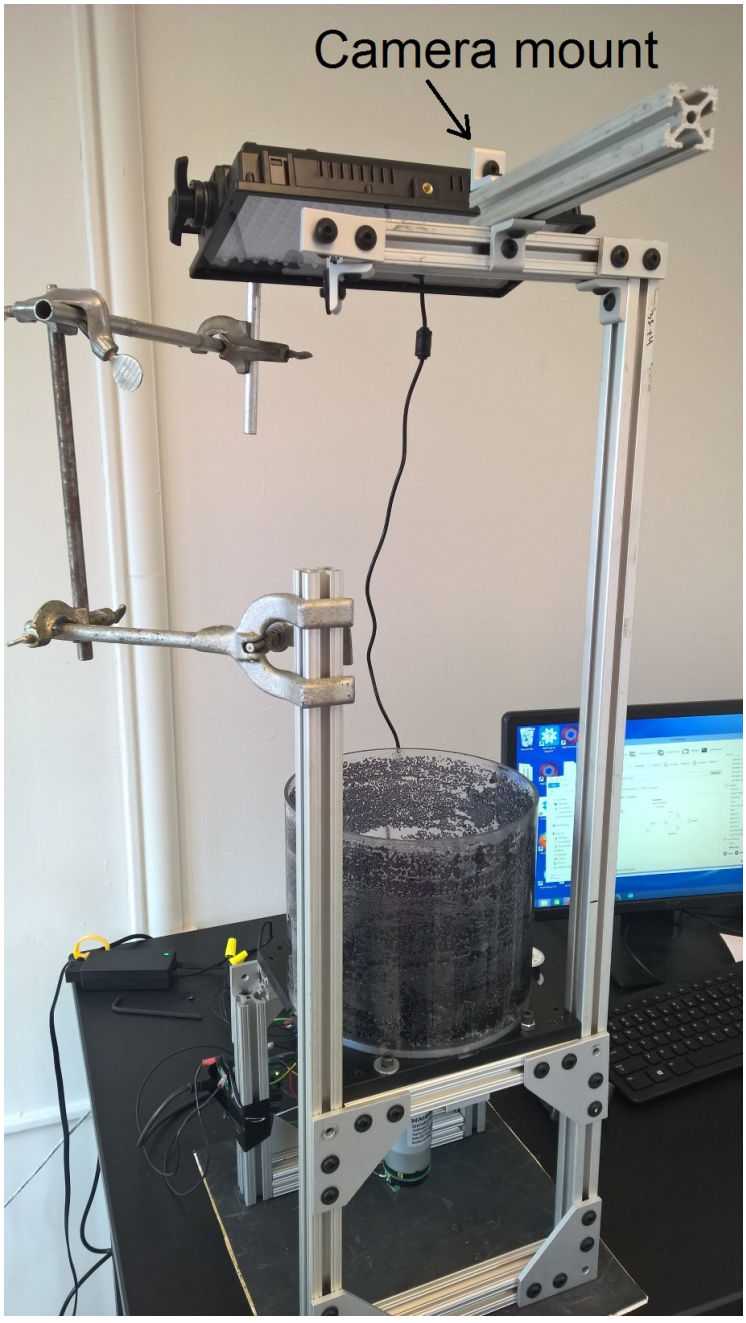

Figure B.5: Flow cell apparatus as built. The metal bar in the upper left is the camera mount.

methods. One possible solution is to replace the gearmotor with a stepper motor, a type of motor that excels at developing high torque at low speeds. Stepper motors would also remove the need for an encoder, as stepper motors rotate a specific amount–a 'step'–when activated. The only components necessary to purchase to convert the flow cell to stepper-motor-based operation would be a stepper motor, an Arduino stepper motor controller board, and mounting hardware to connect the motor to the flow cell and adapter.

B.5 Conclusion

This project was overall a success. The system was able to generate the required flows, and the mounting system for lights and camera was robust and adjustable. While there are some future steps that should be taken to improve the functioning of the flow cell, the current hardware is adequate for performing the kinds of experiments needed for the verification of granular flow models, and it will hopefully enable development of general continuum models of granular flow.